

See discussions, stats, and author profiles for this publication at: <https://www.researchgate.net/publication/320456128>

A Method of Determining Formation Density Based on Fast-Neutron Gamma Coupled Field Theory

Article in PETROPHYSICS · June 2017

CITATIONS

0

READS

209

8 authors, including:



Quanying Zhang

China University of Petroleum

10 PUBLICATIONS 5 CITATIONS

[SEE PROFILE](#)



Feng Zhang

China University of Petroleum

30 PUBLICATIONS 30 CITATIONS

[SEE PROFILE](#)



Juntao Liu

China University of Petroleum

27 PUBLICATIONS 20 CITATIONS

[SEE PROFILE](#)



He Wu

Karlsruhe Institute of Technology

5 PUBLICATIONS 2 CITATIONS

[SEE PROFILE](#)

Some of the authors of this publication are also working on these related projects:



Theory and method of pulsed neutron-gamma density logging [View project](#)

A Method of Determining Formation Density Based on Fast-Neutron Gamma Coupled Field Theory

Quanying Zhang¹, Feng Zhang¹, Juntao Liu¹, He Wu¹, Guoli Wu², Wenbao Jia³, Yongzhou Ti⁴, and Jing Li⁵

ABSTRACT

Pulsed-neutron gamma density (NGD) logging, as an emerging density measurement technology, is of significance for radioprotection and technological development of logging-while-drilling (LWD). Compared to the gamma-gamma density (GGD), the NGD technique has the advantages of environment, safety and health. However, due to the lack of theory, the quantitative relationship between the inelastic gamma field distribution and formation parameters has not been resolved so far. The current data-processing methods are mainly based on the empirical formulas obtained by experiment and simulation methods.

In order to quantitatively clarify the logging mechanism and theoretically develop a new density algorithm, the coupled idea is introduced to NGD logging. Based on the

theories of fast-neutron scattering and gamma attenuation, the fast neutron-gamma coupled field theory is put forward to describe the distribution of inelastic gamma field. The inelastic gamma field distribution is characterized by the inelastic scattering cross section, fast-neutron scattering free path and formation density, and the influence of the formation parameters on the field distribution is quantified and a new density algorithm is derived from the coupled theory. The new density algorithm can avoid the complex correction of hydrogen index and simplify the process of density measurement. In addition, the coupled field theory and the new density algorithm are verified by Monte Carlo simulation. The research not only clarifies the NGD mechanism but also provides theoretical guidance for NGD logging.

INTRODUCTION

Formation density is one of the most important parameter for formation evaluation, particularly in oil and gas exploration. The traditional gamma-gamma density (GGD) employing a Cs-137 radioisotope as a gamma source has raised certain health, safety, and environmental (HSE) concerns. The companies working with radioisotope sources have to follow rigorous standards and suffer enormous cost on the packaging, storage, transportation, handling, and disposal of the materials (Badruzzaman et al., 2004; Alakeely and Meridji, 2014).

With the increasing demand for radioisotope-free logging while-drilling (LWD) operations, it has been an inevitable trend for nuclear logging to measure formation parameters using controllable sources instead of radioisotopes (Xu et al., 2010; Smith et al., 2013; Badruzzaman, 2014; Liu et

al., 2016). Recently introduced pulsed-neutron gamma density (NGD) logging tools have already presented increased advantages in the areas of environment and safety (Wilson, 1995; Neuman et al., 1999). The deuterium-tritium generators produce 14-MeV neutrons, many of which interact with the nuclei of the formation through inelastic collisions. These interactions are typically followed by the emission of a variety of high-energy gamma rays. Similar to the case of the GGD measurement, the transport and attenuation of these gamma rays is a strong function of the formation density. However, the new NGD technology faces several challenges to replace the conventional GGD. The most important is the source issue. The gamma-ray source of a NGD tool is a spatially distributed source of gamma rays that is far from being monoenergetic, while a GGD tool deploys a monoenergetic and collimated point source, enabling very consistent and accurate density measurements.

Manuscript received by the Editor February 7, 2017; revised manuscript received May 30, 2017; manuscript accepted June 6, 2017.

¹School of Geosciences, China University of Petroleum, Qingdao 266580, China; zqy_cn@sina.com; zhfx_y_cn@upc.edu.cn; liujuntao20082009@126.com; easywh@163.com

²College of Science, China University of Petroleum, Qingdao 266580, China; wuguoli81@163.com

³College of Materials Science and Engineering, Nanjing University of Aeronautics and Astronautics, Nanjing 211106, China; jia_wenbao@hotmail.com

⁴Zhengzhou Key Laboratory of Isotope Tracing and Detecting, Isotope Research Institute of Henan Academy of Sciences Co. Ltd, Zhengzhou 450015, China; twstxkj@163.com

⁵Department of Biology, Guta Branch School of Mongolian Senior High School, Chaoyang 122300, China; lijing1028_cn@163.com

Another issue is that the gamma rays have high energy compared to those of the Cs-137. The gamma-ray physics must include significant pair production interactions, which is not considered in GGD measurement. In addition, the extent of the induced-gamma source region depends on the transport of the fast neutrons from the source to the point of gamma-ray production. Besides, the attenuation distance of gamma rays is also closely related to the distance from the points of gamma-ray production to the detector.

Although there are still many difficulties to be overcome, the relevant research has made some remarkable achievements (Mirto et al., 2006). In the early NGD tools, formation density is determined using inelastic gamma rays from oxygen atoms, which has low density accuracy and stability (Wilson et al., 1995). Thereafter, the common method for measuring formation density by the total inelastic gamma-count ratio is raised (Odom et al., 1999), however, the results are greatly influenced by the hydrogen index (HI). In order to improve the NGD accuracy, a series of hydrogen index (HI) correction methods, which are achieved by fast neutron, epithermal neutron, thermal neutron and capture gamma, are studied by experiment and MCNP simulation (Odom et al., 2001a, 2001b; Jacobson et al., 2004; Weller et al., 2005; Reichel et al., 2013; Zhang et al., 2013). However, due to the lack of NGD theory, there has been no significant breakthrough in data-processing methods and quantitative study of the inelastic gamma field distribution.

Recently, coupled theory, which describes the coupling relationship of two or more fields, has been widely used in the field of geological exploration, especially in seismoelectric and electromagnetic exploration (Panzner et al., 2016; Yu et al., 2016). In essence, the inelastic gamma field is also a coupled field of the fast-neutron field and the gamma field. In this paper, the coupled theory is applied to describe the inelastic gamma field distribution. According to the theory of fast-neutron scattering and gamma attenuation, the fast-neutron gamma coupled field theory is proposed to quantify the influence of inelastic scattering cross section, fast-neutron scattering free path and density attenuation on the inelastic gamma field distribution, and a new density algorithm is derived from the coupled theory. Moreover, the fast-neutron gamma coupled theory and the new density algorithm are verified using Monte Carlo simulation. The results of applying the new NGD algorithm in a well simulation are presented.

THEORY OF FAST-NEUTRON GAMMA COUPLED FIELD

Analysis of Formation Nuclear Parameters

The inelastic gamma field distribution is controlled by

two main effects: the gamma-ray generation and attenuation. The inelastic scattering cross section and the mass-attenuation coefficient are basic nuclear parameters that determine the generation and attenuation of inelastic gamma rays. Here, we first discuss the formation nuclear parameters before deriving the field distribution.

The inelastic scattering cross section determines the probability of inelastic collisions between fast neutrons and formation nuclides. Figure 1, from the ENDF/B-VII.0 nuclear database (Chadwick et al., 2006), shows the inelastic scattering cross sections of different formation materials. As shown in Fig. 1, the inelastic scattering cross sections depend on the formation materials and the fast-neutron energy. The probability of inelastic collisions occurring in the energy range from 7.5 to 14.2 MeV is far greater than that in the energy range from 1.0 to 7.5 MeV, which means the inelastic collisions occurring in the higher energy range dominate in the total inelastic collisions. Therefore, the inelastic scattering cross section of the energy range from 7.5 to 14.2 MeV can be viewed as the total neutron inelastic scattering cross section in some cases. Furthermore, the inelastic scattering cross section does not vary much with the fast-neutron energy in the higher energy range.

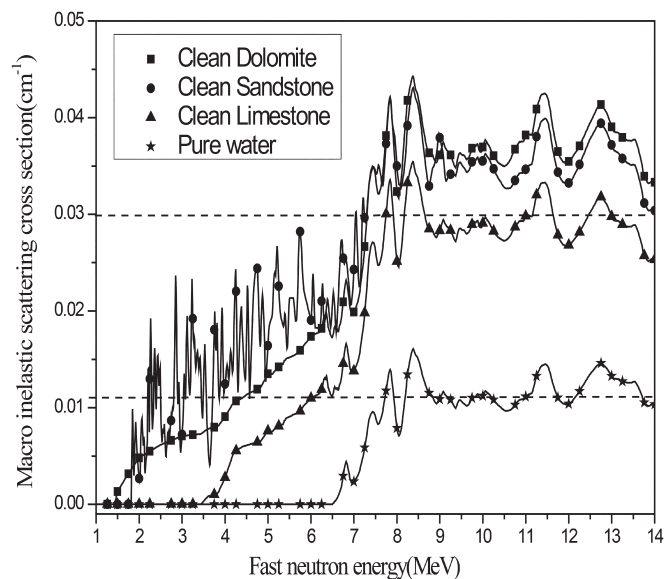


Fig.1—Inelastic scattering cross section of different formation materials.

The formation attenuation of gamma rays is closely tied to the formation density and the mass-attenuation coefficient, where the mass-attenuation coefficient is influenced by the average energy of inelastic gamma rays in the formation. Figure 2 provides the gamma-ray energy levels for oxygen-16, carbon-12, silicon-28 and calcium-40 (Inanc, 2014). Oxygen-16 gamma rays are significantly

more energetic compared to the others and they are mostly in the 6 to 7 MeV range. In contrast, carbon-12 has only one line, around 4.4 MeV. The silicon-28 and calcium-40 gamma lines have much lower energies compared to the oxygen-16 and carbon-12 lines.

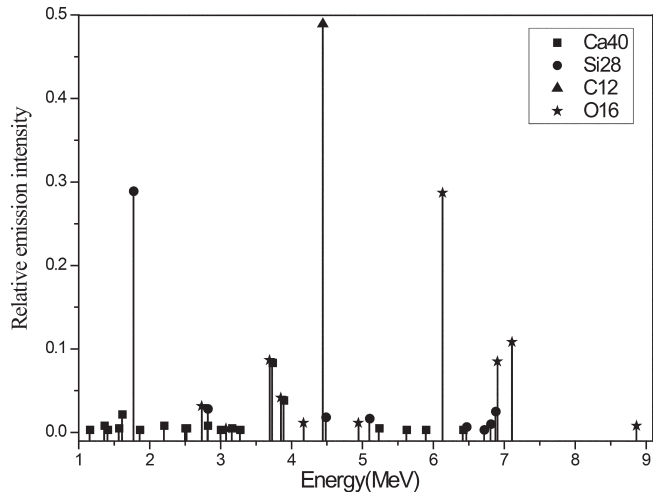


Fig. 2—Gamma-ray emission lines from various nuclides (Inanc, 2014).

According to the formation atomic density and the gamma-ray data from Fig. 2, the average energy levels of inelastic gamma rays for dolomite, sandstone, limestone and water can be derived, they are 5.36-, 5.04 -, 5.25- and 5.73-MeV, respectively. That means the average energy range of inelastic gamma rays in the formation with different lithologies and porosities is 5.04 to 5.73 MeV. In addition, the relationship of the mass-attenuation coefficient and the gamma-ray energy is calculated with XCOM (Berger et al., 2010), shown in Fig. 3. The mass-attenuation coefficients of different formation materials are approximately the same in the energy range of 0.1 to 10 MeV. Changes in the mass-attenuation coefficient in the energy range of 5.04 to 5.73 MeV are so small that they can be regarded as a constant.

Inelastic Gamma Field Distribution in Infinite Uniform Formation

To account for the inelastic gamma field distribution, a spherical model of the infinite and uniform formation is established, as shown in Fig. 4. The neutron source is placed in the center of the model (O) and emits 14.2 MeV fast neutrons into the formation evenly. A spherical surface detector is set to record the inelastic gamma rays from the infinite formation.

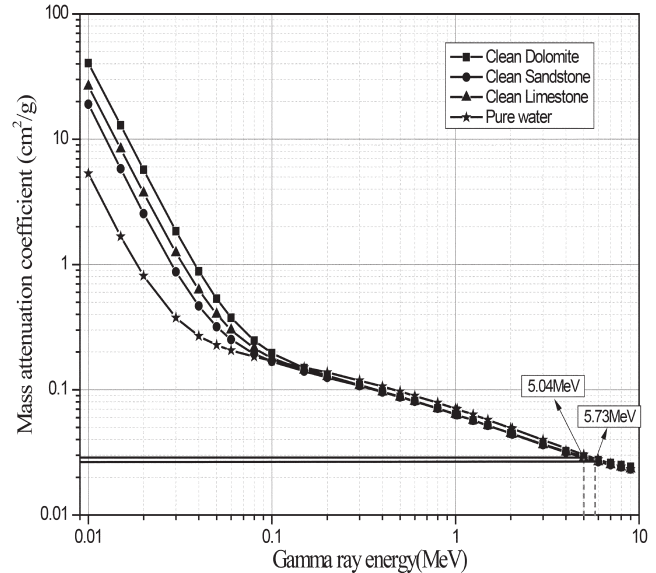


Fig. 3—Relationship between the mass-attenuation coefficient and gamma-ray energy.

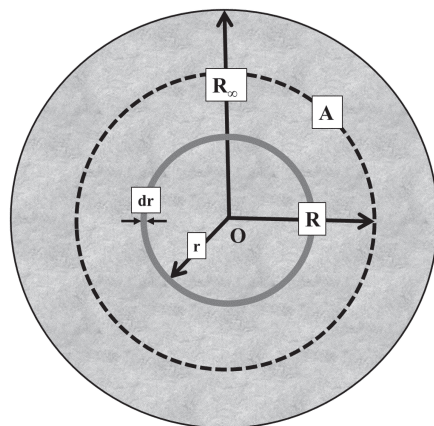


Fig. 4—Schematic model of the infinite uniform spherical formation. The dashed circle with radius R represents the spherical surface detector A, the solid circle with radius r represents the spherical shell with thickness dr and radius r .

According to fast-neutron scattering theory (Tittle et al., 1961), the flux of fast neutrons with inelastic collisions is

$$J(r) = \frac{S_0}{4\pi r^2} e^{-r/\lambda_s}, \quad (1)$$

where λ_s is the fast-neutron scattering free path, which is related to the formation lithology and hydrogen index (HI), S_0 is neutron-source strength, and r is the distance from the source.

In view of the analysis from Fig. 1, we ignore the effect of fast-neutron energy on the inelastic scattering cross section. And the number of inelastic gamma photons generated in the spherical shell with thickness dr and radius r is expressed as

$$dI(r) = i\Sigma_{in} 4\pi r^2 J_f(r) dr = i\Sigma_{in} S_0 e^{-r/\lambda_s} dr, \quad (2)$$

where i is the average number of gamma photons from inelastic collisions of a fast neutron, and Σ_{in} is the inelastic scattering cross section, which depends on the formation material.

The formation attenuation needs to be considered on the transport of the gamma rays from their origin to the detector. Referring to the analysis of the mass-attenuation coefficient (Fig. 3), we assume that the mass-attenuation coefficient of inelastic gamma rays is not affected by the formation lithology and porosity. The number of inelastic gamma photons generated in the spherical shell with radius r and recorded by detector A can be given as

$$dI'(r) = dI(r)e^{-\rho\mu_m|r-R|} = i\Sigma_{in} S_0 e^{-r/\lambda_s} e^{-\rho\mu_m|r-R|} dr, \quad (3)$$

where ρ is the formation density.

The total number of gamma photons from the infinite formation detected by the detector is calculated by the integration

$$I'(R) = \int_0^\infty dI'(r) = i\Sigma_{in} S_0 \int_0^\infty e^{-r/\lambda_s} e^{-\rho\mu_m|r-R|} dr. \quad (4)$$

Finally, the inelastic gamma field distribution in infinite uniform formation can be described as follows

$$J(R) = \frac{I'(R)}{4\pi R^2} = \frac{i\Sigma_{in} S_0}{4\pi R^2} \left(\frac{2\rho\mu_m e^{-R/\lambda_s} - (\rho\mu_m + 1/\lambda_s) e^{-\rho\mu_m R}}{(\rho\mu_m)^2 - 1/\lambda_s^2} \right). \quad (5)$$

It can be seen from Eq. 5 that the inelastic gamma field distribution is determined by the parameters, such as the distance from the source R (referred to the detector spacing in the following study), inelastic scattering cross section Σ_{in} , fast-neutron scattering free path λ_s , formation density ρ , and so on.

Field Distribution in the Logging Condition

The inelastic gamma field distribution in NGD logging can also be described by the coupled field theory. And the coupled theory can be more practical for logging applications, if we make some adjustments with reference to the logging condition.

According to the model shown in Fig. 1, the inelastic gamma photons detected by the detector can be divided into two parts: one from the formation between the source and the detector, and the other from the formation outside the detector. And Eq. (5) can be expressed as follows

$$J_{inner}(R) = \frac{i\Sigma_{in} S_0}{4\pi R^2} \int_0^R e^{-r/\lambda_s} e^{-\rho\mu_m(R-r)} dr = \frac{i\Sigma_{in} S_0}{4\pi R^2} \left(\frac{e^{-R/\lambda_s} - e^{-\rho\mu_m R}}{\rho\mu_m - 1/\lambda_s} \right) (0 < r < R) \quad (6)$$

$$J_{outer}(R) = \frac{i\Sigma_{in} S_0}{4\pi R^2} \int_R^\infty e^{-r/\lambda_s} e^{-\rho\mu_m(r-R)} dr = \frac{i\Sigma_{in} S_0}{4\pi R^2} \left(\frac{e^{-R/\lambda_s}}{\rho\mu_m + 1/\lambda_s} \right) (R \leq r < \infty), \quad (7)$$

where J_{inner} and J_{outer} are the gamma-count contributions of the formation inside and outside the detector. By the Monte Carlo method, Fig. 5 gives the inelastic-gamma-flux contribution for the detectors with different detector spacing. Figure 5a shows the inelastic contributions near the source are more important to the detector response for the saturated formations. Figure 5b shows the contribution proportion of the region between the source and the detector is much larger than that of the region outside the detector, and the proportion of the contribution of the inner region increases with the increasing detector spacing. When the spacing is greater than 30 cm, the contribution will exceed 90%.

In actual logging, the tool shell, drill collar and borehole water will further strengthen the slowing-down and inelastic scattering capability of fast neutrons, which leads to an obvious increase in the contribution of gamma count near the source. Therefore, when source-detector distance is long enough (≥ 30 cm), Eq. 5 can be simplified as

$$J_{in}(R) \approx \frac{i\Sigma_{in} S_0}{4\pi R^2} \left(\frac{e^{-R/\lambda_s} - e^{-\rho\mu_m R}}{\rho\mu_m - 1/\lambda_s} \right), \quad (8)$$

where $\rho\mu_m$ is always less than $1/\lambda_s$ in gas- or water-saturated formations.

According to the Lagrange mean value theorem, Eq. 8 can be rewritten as

$$J_{in}(R) = \frac{i\Sigma_{in} S_0}{4\pi R^2} \frac{[-Re^{-R\xi} (1/\lambda_s - \rho\mu_m)]}{\rho\mu_m - 1/\lambda_s} = \frac{i\Sigma_{in} S_0}{4\pi R} e^{-R\xi}, \quad (9)$$

where ξ belongs to the interval $(\rho\mu_m, 1/\lambda_s)$ and is defined as

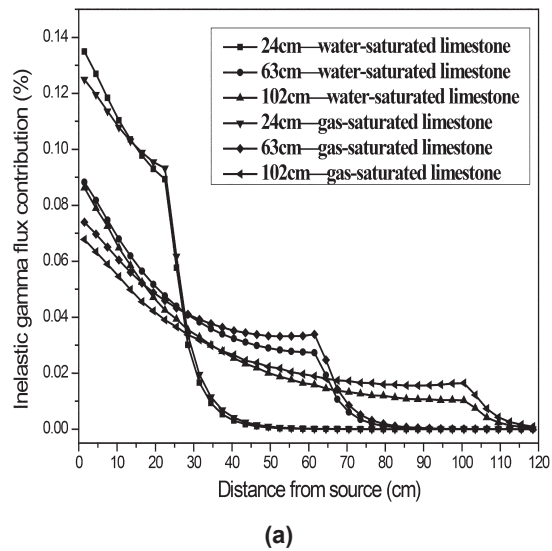
$$\xi = 1/\lambda_s - \alpha(1/\lambda_s - \rho\mu_m) \quad \alpha \in (0, 1), \quad (10)$$

where α is the proportional coefficient, which is used to describe the relative position of ξ .

Eliminating ζ from Eqs. 9 and 10, we obtain

$$J_{in}(R) = \frac{i\Sigma_{in} S_0}{4\pi R} e^{-R(1-\alpha)(1/\lambda_s)} e^{-R\rho\mu_m} \quad (11)$$

The proportional coefficient α in Eq. 11 is a function of the formation condition and detector spacing. Figure 6 shows the relationship of the coefficient α and formation porosity under different detector spacings. The range in the change of coefficient α with formation porosity increases with the increasing detector spacing. However, the value of coefficient α only changes from 0.5 to 0.55 in the water-saturated formation when the spacing reaches 70 cm, and the change range is even smaller in the gas-saturated formation, which means the effect of formation porosity on coefficient α can be ignored to a certain extent.



(a)

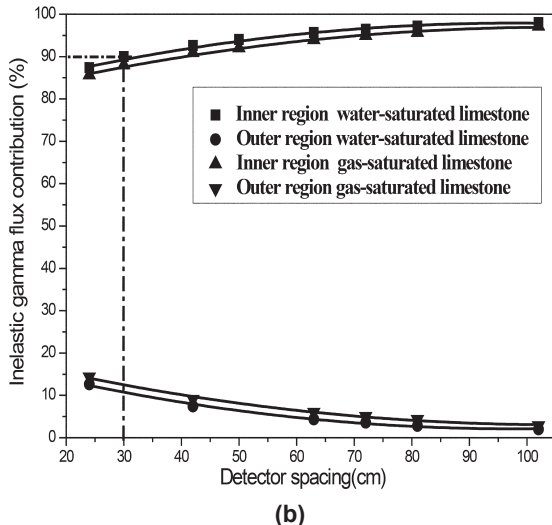


Fig. 5—Inelastic-gamma-flux contribution for detectors with different spacings: (a) inelastic-gamma-flux contribution, (b) the contribution proportion of the inner and outer formation. The formation is set to a water-saturated limestone (20 p.u., 2.368 g/cm^3) and a gas-saturated limestone (20 p.u., 2.208 g/cm^3), respectively.

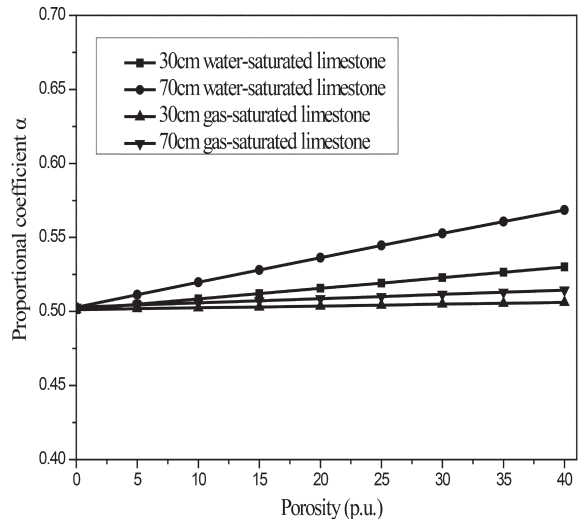


Fig. 6—Relationship of the coefficient α , detector spacing R , and formation porosity. The formation is a water-saturated or gas-saturated limestone. And the density and fast-neutron scattering free path changes simultaneously with the formation porosity.

For the convenience of calculation, we can attribute the change in coefficient α to the change of the spacing R and neglect the effect of formation condition, based on the analysis of Fig. 6. The calculated results of the above assumption are compared with those of Eq. 8 in Fig. 7. It can be seen that the results of the assumption are in good agreement with those of Eq. 8, and the relative error of the two algorithms is less than 3%. That means Eq. 11 can be used to describe inelastic gamma field distribution in NGD logging instead of Eq. 8.

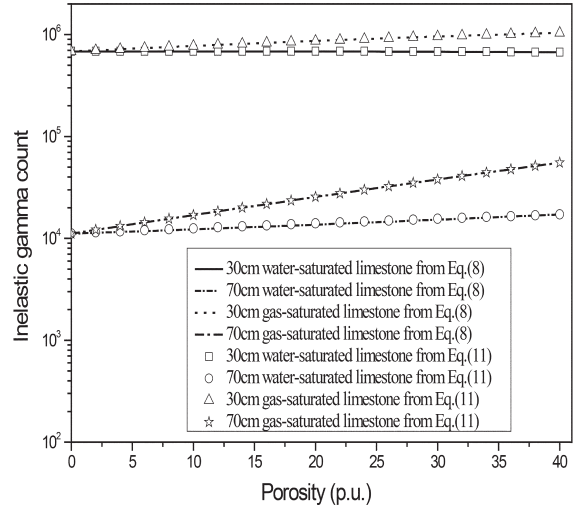


Fig. 7—Comparison of results of the inelastic gamma counts from Eqs. 8 and 11. The coefficient α used for the calculation in Eq. 11 is the proportional coefficient in the 40-p.u. water-saturated and gas-saturated formation, and it varies only with the detector spacing but does not vary with the formation condition.

Influence of the Single Nuclear Parameters

To clarify the influence of the inelastic scattering cross section Σ_{in} , fast-neutron scattering free path λ_s , and density attenuation on the inelastic gamma field distribution, we take the natural logarithm for Eq. 12,

$$\ln J_{in} = -R(1-\alpha) \left(\frac{1}{\lambda_s} \right) - R\rho\mu_m + \ln \left(\frac{i\Sigma_{in}S_0}{4\pi R} \right). \quad (12)$$

In the water-saturated formation, the inelastic scattering cross section Σ_{in} and density ρ are both the functions of porosity ϕ ,

$$\rho = \phi\rho_w + (1-\phi)\rho_{ma} \quad (13)$$

$$\Sigma_{in} = \phi\Sigma_{in,w} + (1-\phi)\Sigma_{in,ma}, \quad (14)$$

where ρ_w and ρ_{ma} are water and formation matrix density, respectively, $\Sigma_{in,w}$ and $\Sigma_{in,ma}$ are the inelastic scattering cross sections of water and formation matrix, respectively.

Eliminating the ϕ from Eqs. 13 and 14, the mathematical relationship of Σ_{in} and ρ is obtained

$$\Sigma_{in} = \frac{\rho(\Sigma_{in,ma} - \Sigma_{in,w}) + \rho_{ma}\Sigma_{in,w} - \rho_w\Sigma_{in,ma}}{\rho_{ma} - \rho_w} \quad (15)$$

From Eq. 15 it can be seen that the inelastic scattering cross section increases simultaneously with increasing density. That is because the inelastic scattering cross section of the matrix is usually larger than that of the fluid.

The derivatives of Eq. 12 with respect to ρ and λ_s are derived, respectively, to describe the influence of inelastic scattering cross section, density attenuation and fast-neutron scattering,

$$\frac{\partial \ln J_{in}}{\partial \rho} = -R\alpha\mu_m + \frac{\Sigma_{in,ma} - \Sigma_{in,w}}{\rho(\Sigma_{in,ma} - \Sigma_{in,w}) + \rho_{ma}\Sigma_{in,w} - \rho_w\Sigma_{in,ma}} \quad (16)$$

$$\frac{\partial \ln J_{in}}{\partial \lambda_s} = \frac{R(1-\alpha)}{\lambda_s^2}, \quad (17)$$

where the first term on the right side of Eq. 16 represents the effect of the density attenuation, and the second term is the effect of the inelastic scattering cross section. Equation 17 represents the effect of the fast-neutron scattering free path λ_s . From Eqs. 16 and 17, it can be seen that the effects of density attenuation and fast-neutron scattering free path on the inelastic gamma field both increase with increasing detector spacing R . However, the effect of Σ_{in} on the inelastic gamma field distribution is not affected by the detector spacing.

In addition, we can see from Eq. 16 that the effects of density attenuation and inelastic scattering cross section

are opposite. When the fast-neutron scattering free path λ_s is constant, the effects of density attenuation and inelastic scattering cross section increase simultaneously with the increasing density, and these two effects will reach a balance in a special detector spacing, R_0 . For a detector spacing $< R_0$ the inelastic scattering cross section effect dominates the gamma field, the inelastic gamma flux increases with the increasing density. For a detector spacing $> R_0$, the density-attenuation effect dominates the gamma field, the inelastic gamma flux decreases with the increasing density. According to Eq. 16, R_0 can be obtained when the equation is set to zero,

$$R_0 = \frac{\Sigma_{in,ma} - \Sigma_{in,w}}{[\rho(\Sigma_{in,ma} - \Sigma_{in,w}) + \rho_{ma}\Sigma_{in,w} - \rho_w\Sigma_{in,ma}] \alpha\mu_m}. \quad (18)$$

Equation 18 indicates that R_0 is not constant and changes with the density, lithology and the coefficient α ; and according to Eq. 18, the R_0 value for different lithologies, porosities, and pore fluids can be given in Fig. 8.

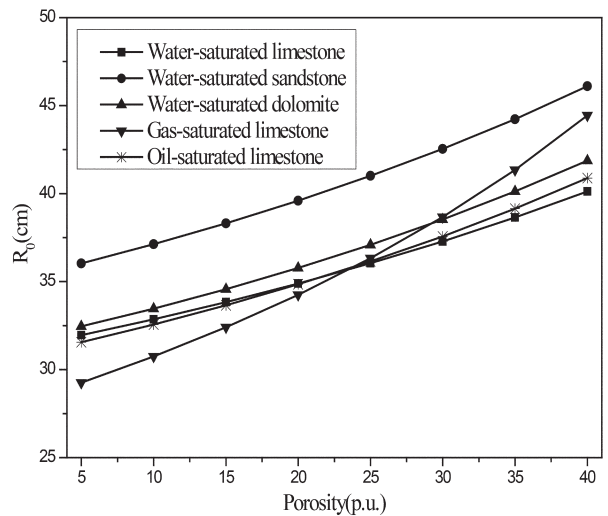


Fig. 8—Quantitative calculation of the R_0 value for different lithologies, porosities, and pore fluids.

As shown in Fig. 8, the R_0 value changes with formation lithology, porosity and both the pore fluid and R_0 increase as the formation porosity increases. However, due to the limitation of formation parameters, the R_0 value only changes in a limited range for the common formation. For example, the water-filled limestone the R_0 value is between about 32 and 40 cm. Once the detector spacing exceeds the maximum of R_0 , the density-attenuation effect will always dominate the gamma field, and the effect of the inelastic scattering cross section will be masked.

METHOD OF DETERMINING DENSITY

Assuming that the detector spacing is L , and the density algorithm of the single gamma detector can be obtained from Eq. 12

$$\rho = -\frac{1}{L\alpha\mu_m} \ln J_{in} - \frac{L(1-\alpha)}{L\alpha\mu_m} \frac{1}{\lambda_s} + \frac{1}{L\alpha\mu_m} \ln(i\Sigma_m S_0) - \frac{\ln(4\pi L)}{R\alpha\mu_m}. \quad (19)$$

Equation 19 shows that determining density by the single gamma detector needs to measure the inelastic scattering cross section Σ_{in} , fast-neutron scattering free path λ_s , and other parameters simultaneously. Unfortunately, it is very difficult to directly measure i , Σ_{in} , and λ_s using logging tools.

Based on the density algorithm of the single detector, we develop a new density algorithm by combining the gamma information from the near and far detectors. Assume that the detector spacings of the near and far detectors are L_1 and L_2 , respectively. The single-detector density algorithm using the near or far detector, respectively, can be given as

$$\rho = -\frac{1}{L_1\alpha_1\mu_m} \ln J_{in1} - \frac{L_1(1-\alpha_1)}{L_1\alpha_1\mu_m} \frac{1}{\lambda_s} + \frac{1}{L_1\alpha_1\mu_m} \ln(i\Sigma_m S_0) - \frac{\ln(4\pi L_1)}{L_1\alpha_1\mu_m} \quad (20)$$

$$\rho = -\frac{1}{L_2\alpha_2\mu_m} \ln J_{in2} - \frac{L_2(1-\alpha_2)}{L_2\alpha_2\mu_m} \frac{1}{\lambda_s} + \frac{1}{L_2\alpha_2\mu_m} \ln(i\Sigma_m S_0) - \frac{\ln(4\pi L_2)}{L_2\alpha_2\mu_m}, \quad (21)$$

where J_{in1} and J_{in2} are the gamma counts of the near and far detectors, respectively. α_1 and α_2 are the proportional coefficients of the near and far detectors, respectively.

Eliminating $\ln(i\Sigma_m S_0)$ from Eqs. 20 and 21, we obtain the new density algorithm

$$\rho = -\frac{1}{(L_1\alpha_1 - L_2\alpha_2)u_m} \ln(J_{in1}/J_{in2}) - \frac{[L_1(1-\alpha_1) - L_2(1-\alpha_2)]}{(L_1\alpha_1 - L_2\alpha_2)u_m} \frac{1}{\lambda_s} + \frac{\ln(L_2/L_1)}{(L_1\alpha_1 - L_2\alpha_2)u_m}. \quad (22)$$

According to the new density algorithm, the formation density can be determined by the fast-neutron scattering free path, λ_s , and the inelastic gamma counts of the near and far detectors, where λ_s can be characterized by other parameters, such as fast neutrons, thermal neutrons and capture gamma rays.

Taking the fast-neutron characterization as an example, the fast-neutron scattering free path can be characterized by the fast-neutron flux (Tittle et al., 1961)

$$\ln J_f(L_3) = -L_3 \left(\frac{1}{\lambda_s} \right) + \ln \frac{4\pi L_3^2}{S_0}, \quad (23)$$

where L_3 is the fast-neutron detector spacing.

Substituting Eq. 23 into Eq. 22, we obtain

$$\begin{aligned} \rho = & -\frac{\ln(J_{in1}/J_{in2})}{(L_1\alpha_1 - L_2\alpha_2)u_m} + \frac{[L_1(1-\alpha_1) - L_2(1-\alpha_2)]}{L_3(L_1\alpha_1 - L_2\alpha_2)u_m} \ln J_f + \\ & \frac{[L_1(1-\alpha_1) - L_2(1-\alpha_2)]}{L_3(L_1\alpha_1 - L_2\alpha_2)u_m} \ln \frac{4\pi L_3^2}{S_0} + \frac{\ln(L_2/L_1)}{(L_1\alpha_1 - L_2\alpha_2)u_m}. \end{aligned} \quad (24)$$

When the detector spacing is fixed, Eq. 24 is rewritten as

$$\rho = A \ln(\phi_{in1}/\phi_{in2}) + B \ln \phi_f + C, \quad (25)$$

where A, B and C are constants associated with the detector-spacing. Note that the new algorithm can determine formation density by measuring the fast-neutron count and the near-to-far detector gamma-count ratio, which avoids the need for a HI correction and simplifies the data processing.

MONTE CARLO SIMULATION

Monte Carlo N-particle (MCNP) transport code (X-5 Monte Carlo Team, 2008) has been widely applied in studies to optimize the parameters, logging responses and other aspects of nuclear logging instruments (Briesmeister, 1986, Gardner and Xu, 2009; Oden et al., 2006; Liu et al., 2014). In order to verify the coupled field theory and the new density algorithm, the MCNP code is used to build the NGD tool model.

As shown in Fig. 9, the tool consists of a D-T source, two gamma detectors and one fast-neutron detector. The 20-cm borehole is filled with fresh water. The detector spacings of the near and far gamma detectors are 35 and 65 cm, respectively. Shielding materials are located between the neutron source and the detector and between the near and far detectors. The tool is placed in the drill collar and pressed against the borehole wall. The working time of the D-T source is 0 to 20 μ s, the time windows of gamma rays and fast neutrons are both 0 to 20 μ s, the energy windows of the gamma rays and fast neutrons are 0.01 to 8.5 MeV and 1.0 to 14.0 MeV, respectively.

The Density Response of Inelastic Gamma Count in Different HI Conditions

The formation is a water-saturated limestone. Formation HI is set to 0.01, 0.1, 0.2, 0.3 and 0.4. The formation density is varied in a small range (± 0.15 g/cm³) for the constant formation HI. The density responses of the near and far inelastic gamma-detector counts for the different formation HI conditions are shown in Fig. 10.

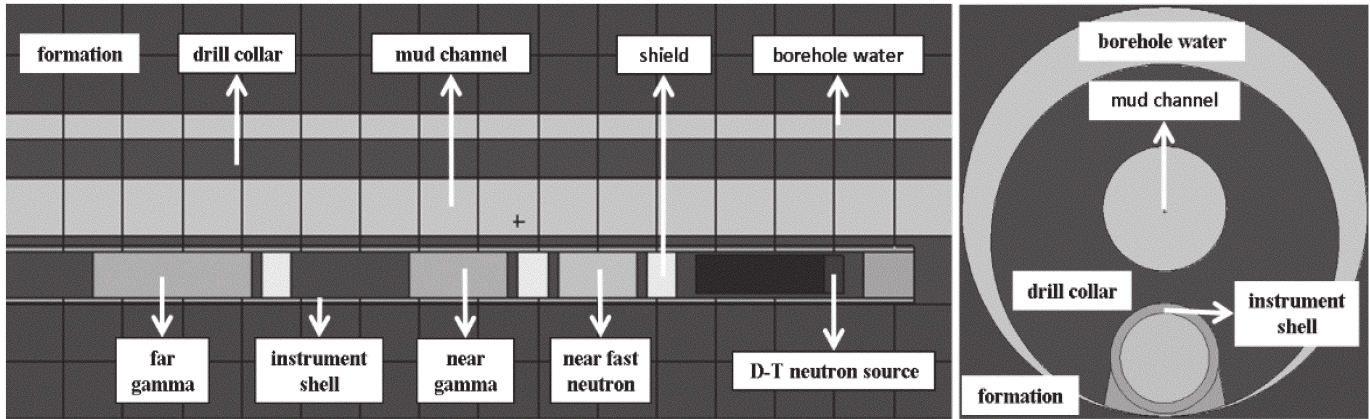


Fig. 9—Monte Carlo simulation model.

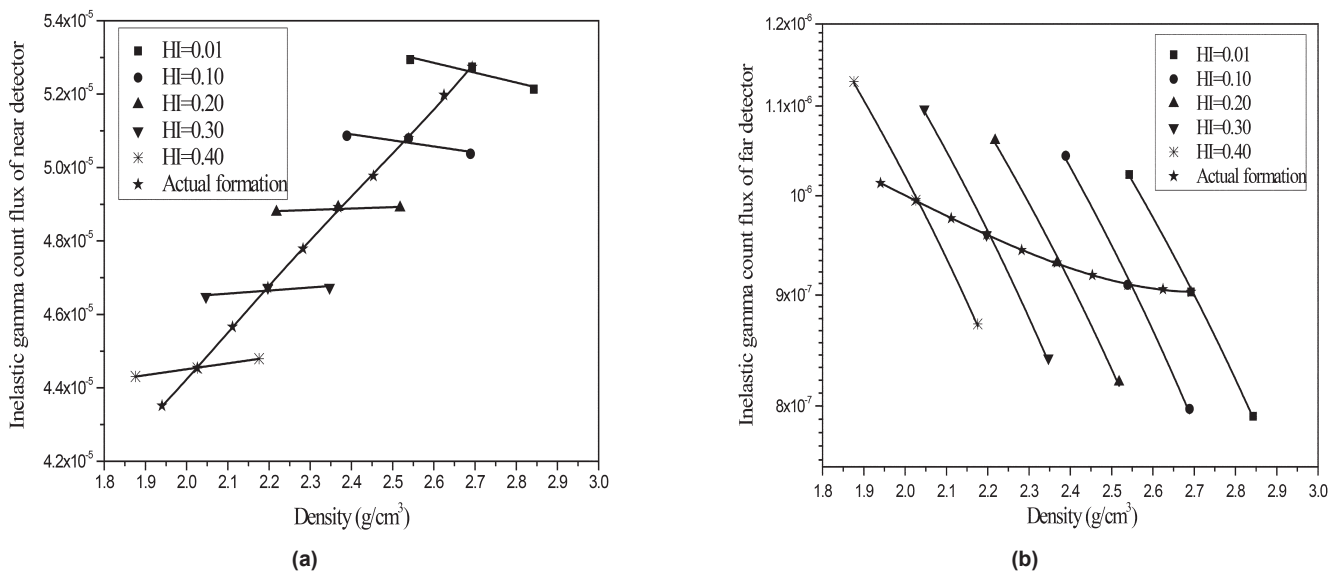


Fig. 10—The density responses of inelastic gamma counts in different HI conditions: (a) the inelastic gamma density response of the near detector; (b) the inelastic gamma density response of the far detector.

Figure 10a shows that the inelastic scattering cross section and density attenuation both have considerable influence on the inelastic gamma count of the near detector. That is because the near-detector spacing is very close to R_0 (mentioned in Eq. 18). As the formation density increases, the effects of the inelastic scattering cross section and density attenuation increase simultaneously. Consequently, two different phenomena appear when the HI is constant: one is that the gamma count increases with the increasing density and the other is that the gamma count decreases. Figure 10b shows that for the far detector, the formation attenuation has the primary influence on gamma count and the influence of inelastic scattering cross section is masked. When the HI is identical, the inelastic gamma count decreases with the increasing density. Furthermore, the effect of HI on the

inelastic gamma count is rather obvious. When density is identical, the slowing-down effect of fast neutrons increases with the increasing HI and the inelastic gamma count decreases. Note that the above phenomena, shown in Fig. 10, have been well explained by the analysis from Eqs. 16 to 18.

Similarly, the density response of the inelastic gamma-count ratio is also studied. Figure 11 shows the density response of the gamma-count ratio in the different HI conditions. The inelastic scattering cross section, Σ_{in} , has little influence on the gamma-count ratio. The gamma-count-ratio curves in the different HI conditions have the same density sensitivity, and the intercept of these curves changes with the formation HI. The simulation results are consistent with those from Eq. 22.

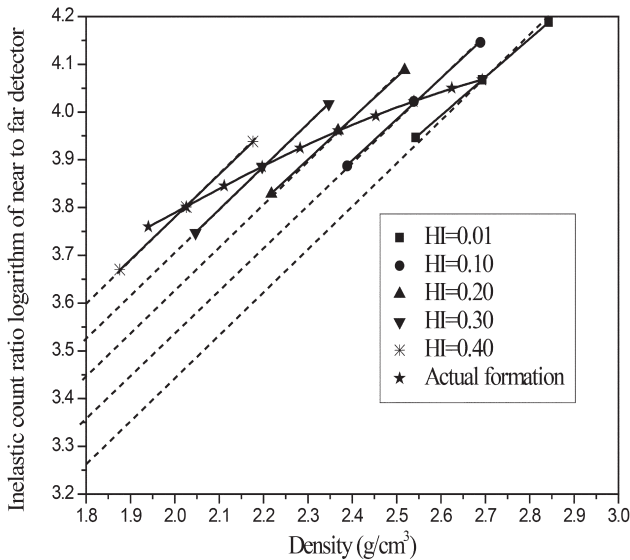


Fig. 11—Density responses of inelastic gamma-count ratio in the different HI conditions.

New NGD Density Algorithm

According to the Eq. (22), the density response of inelastic gamma-count ratio can be expressed as

$$\rho = 1.1185 \ln(J_{in1}/J_{in2}) + f(\lambda_s), \quad (26)$$

where $f(\lambda_s)$ is the intercept of density curve, which has a linear relationship with $(1/\lambda_s)$.

According to the new NGD density algorithm, the fast-neutron count can be used to characterize the intercept $f(\lambda_s)$ instead of λ_s . Figure 12 shows the relationship between the fast-neutron flux and density in the different HI conditions. It can be seen that, for a given porosity, the fast-neutron count close to the source is almost unaffected by the formation density, and it is mainly determined by the HI (or λ_s).

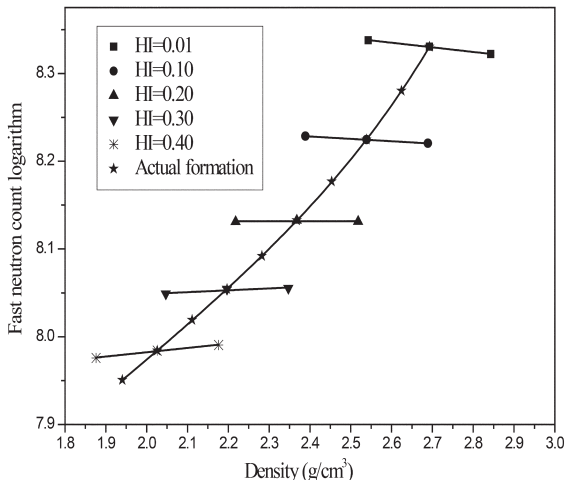


Fig. 12—Density responses of fast-neutron count in the different HI conditions.

According to Eqs. 22 and 23, there is a linear relationship between the intercept $f(\lambda_s)$ and, which has been proved by the simulation data in Fig. 13.

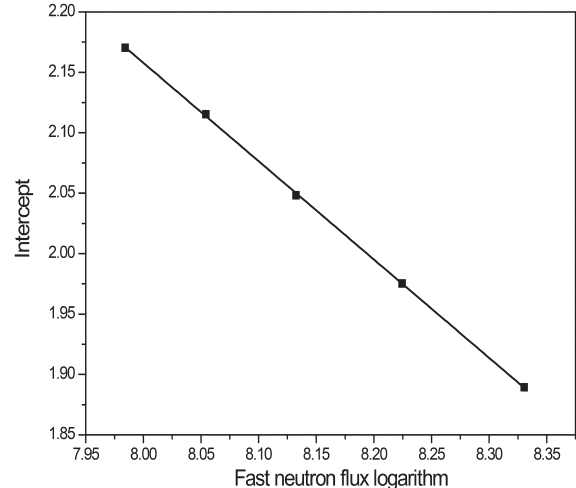


Fig. 13—The relationship of intercept $f(\lambda_s)$ and fast-neutron flux.

The intercept $f(\lambda_s)$ and the fast-neutron logarithm $\ln \phi_f$ show a good linear relationship,

$$f(\lambda_s) = 1.091(\ln J_f) - 10.929. \quad (27)$$

Substituting Eq. 27 into Eq. 26, the new density algorithm is obtained:

$$\rho = 1.1185 \ln(J_1/J_2) + 1.091(\ln J_f) - 10.929. \quad (28)$$

The density results of the new density algorithm are shown in Fig. 14. The formation density obtained by the new algorithm is consistent with the actual formation density, and the density results are no longer affected by the formation HI.

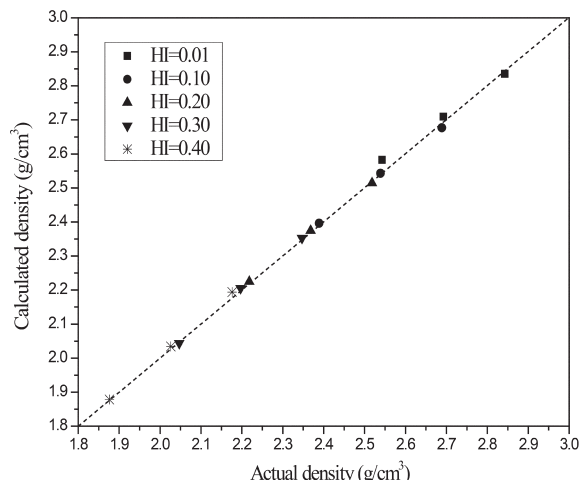


Fig. 14—Data-processing results.

APPLICABILITY OF THE DENSITY ALGORITHM

In this section, the applicability of the new density algorithm in different wellbore and formation conditions is discussed. The density algorithm is calibrated by the simulated data from the 5-, 15-, 25-, and 35-p.u. water-saturated limestone. The effects of borehole fluid, borehole size, lithology and pore fluid on the density algorithm are examined.

Formation HI

The formation is set to a water-saturated limestone. Table 1 shows the results of the new density algorithm in the different HI formations.

Table 1—Results of the New Density Algorithm in Different HI Conditions

Actual HI	Actual Density (g/cm ³)	Calculated Density (g/cm ³)	Error (g/cm ³)
0.01	2.8429	2.8287	0.014
0.2	2.218	2.2236	-0.006
0.3	2.047	2.0415	0.006
0.4	2.176	2.1802	-0.004
0.5	1.855	1.8728	-0.018
0.6	1.684	1.7064	-0.022

From Table 1 it can be seen that the formation HI has little effect on the density algorithm. No matter how the HI changes, the density derived by the new algorithm always matches the actual density. Furthermore, the new density algorithm can perform well in the higher HI formations, and the density errors are less than 0.03 g/cm³.

Formation Lithology

The formation lithology is set to limestone, sandstone and dolomite, respectively. Formation pores are filled with pure water and formation porosity is varied from 0 to 40

p.u. The results of applying the new method in the different lithologies are shown in Table 2.

As shown in Table 2, the formation lithology has little effect on the density results. That is because the formation lithology mainly affects the inelastic scattering cross section, Σ_{in} , and the fast-neutron scattering free path, λ_s . The effect of Σ_{in} is eliminated by the gamma-count ratio and the effect of λ_s on the gamma-count ratio is expressed by the fast-neutron flux. Therefore, the results of the new method are minimally affected by the formation lithology. Of course, there are slight differences on the density results in the different lithology formations, due to the difference of the mass-attenuation coefficient (mentioned in Fig. 3), however, the density differences are small and do not have a significant affect on the actual logging.

Pore Fluid

The formation is limestone. Formation pores are filled with fresh water, methane gas (0.2 g/cm³), and oil (0.8 g/cm³), respectively. The formation porosity is varied from 0 to 40 p.u. and the interval porosity is 5 p.u. Table 3 shows the results of applying the new method in the water-, gas- and oil-saturated formations.

As shown in Table 3, the formation fluid also has little effect on the density results. Similar to the formation lithology, the formation fluid also affects the inelastic-scattering cross section, Σ_{in} , and the fast-neutron scattering free path, λ_s . For the same reason, the effect of formation fluid on the results of the new method are minimal.

Borehole Size

The formation is a water-saturated limestone. The borehole is filled with pure water. The borehole size is set to 20-, 24- and 31-cm, respectively. The porosity is varied from 0 to 40 p.u. The results are presented in Table 4.

Table 2—Results of Applying the New Density Algorithm in Different Lithology Formations

Porosity (p.u)	Limestone		Sandstone		Dolomite	
	Actual Density (g/cm ³)	Error (g/cm ³)	Actual Density (g/cm ³)	Error (g/cm ³)	Actual Density (g/cm ³)	Error (g/cm ³)
5	2.6245	0.0022	2.5675	0.0192	2.7785	0.0019
10	2.5390	0.0046	2.4850	0.0148	2.6822	-0.0008
15	2.4535	-0.0137	2.4025	0.0123	2.5920	0.0025
20	2.3680	0.0144	2.3200	0.0047	2.5010	0.0050
25	2.2825	-0.0013	2.2375	0.0092	2.4161	0.0136
30	2.1970	0.0004	2.1550	0.0073	2.3247	0.0157
35	2.1115	-0.0021	2.0725	0.0083	2.2354	0.0199
40	2.0260	0.0008	1.9900	0.0067	2.1496	0.0276

Table 3—Density Results of the Water-, Gas- and Oil-Saturated Formations

Porosity (p.u)	Pure Water (1.0 g/cm ³)		Methane Gas (0.2 g/cm ³)		Oil (0.8 g/cm ³)	
	Actual Density (g/cm ³)	Error (g/cm ³)	Actual Density (g/cm ³)	Error (g/cm ³)	Actual Density (g/cm ³)	Error (g/cm ³)
5	2.6245	0.0022	2.5845	0.0064	2.6145	-0.0135
10	2.539	0.0046	2.459	0.0155	2.519	-0.0077
15	2.4535	-0.0137	2.3335	0.0143	2.4235	-0.0091
20	2.368	0.0144	2.208	0.0156	2.328	-0.0064
25	2.2825	-0.0013	2.0825	0.0133	2.2325	0.0035
30	2.197	0.0004	1.957	0.0121	2.137	0.0043
35	2.1115	-0.0021	1.8315	0.0034	2.0415	0.0063
40	2.026	0.0008	1.706	-0.0113	1.946	0.0190
45	1.9405	-0.0010	1.5805	-0.0276	1.8505	0.0245

Table 4—Density Results in Different Boreholes

Porosity (p.u)	Actual Density (g/cm ³)	Borehole Size (cm)		
		20	24	31
		Error (g/cm ³)	Error (g/cm ³)	Error (g/cm ³)
5	2.6245	0.0022	0.0606	0.1309
10	2.539	0.0046	0.0596	0.1224
15	2.4535	-0.0137	0.0591	0.1092
20	2.368	0.0144	0.0532	0.1057
25	2.2825	-0.0013	0.0472	0.095
30	2.197	0.0004	0.0484	0.0861
35	2.1115	-0.0021	0.0441	0.0766
40	2.026	0.0008	0.0348	0.0726

As shown in Table 4, borehole size has a significant impact on the density measurement. The density error increases with the increasing borehole size and decreases with the increasing porosity. That is because the density derived from the NGD logging is the average density in a certain area. With the increasing borehole, the borehole water replaces the formation around the wellbore. As a result, the average density decreases and the density error increases. Furthermore, with the increasing porosity, the density differences between formation and borehole water become small, so the density errors become small.

Borehole Fluid

The formation is a water-saturated limestone, borehole size is 20 cm, and the borehole fluid is set to pure water, oil and gas, respectively. The density results for the different borehole fluid conditions are shown in Table 5.

As shown in Table 5, the borehole fluid has a significant impact on the density measurement. For a given porosity, the density errors are greatest when the borehole is filled with gas, and the error is relatively small when the borehole fluid is oil. That is because the oil density and the water density are very close, while the gas density and the water density are significantly different.

Table 5—Density Results in Different Borehole-Fluid Conditions

Porosity (p.u)	Actual Density (g/cm ³)	Borehole Fluid		
		Water	Oil	Gas
		Error (g/cm ³)	Error (g/cm ³)	Error (g/cm ³)
5	2.6245	0.0022	-0.0423	-0.2273
10	2.539	0.0046	-0.0265	-0.233
15	2.4535	-0.0137	-0.0223	-0.2288
20	2.368	0.0144	-0.0419	-0.216
25	2.2825	-0.0013	-0.0331	-0.2236
30	2.197	0.0004	-0.0444	-0.2032
35	2.1115	-0.0021	-0.0401	-0.1991
40	2.026	0.0008	-0.0213	-0.2065

CASE STUDY

A simulation was carried out by the Monte Carlo method. The LWD neutron-gamma tool, shown in Fig. 15, is placed in a 45-m well. The borehole is filled with fresh water and its diameter is 200 mm. The formation used in the simulation consists of four formation layers with different lithology, porosity, pore fluids and density (see Table 6).

Table 6—Parameters of the Formation Layers Used in the Simulation

Formation Type	Lithology	V _{sh} (%)	Porosity (p.u.)	Density (g/cm ³)
A	Water-saturated sandstone	20	30	2.065
B	Water-saturated limestone	10	10	2.488
C	Gas-saturated sandstone	5	20	2.055
D	Clay	90	5	2.1625

The tool is slowly lowered in the borehole from the top of the formation to the bottom and pressed against the borehole wall during the measurement. The midpoint of the near and far gamma detectors is set as the reference point for the density measurement. The results of the simulation are shown in Fig. 15. Data for the original formation are displayed in Tracks 1 and 2, and the calculated density and density error are shown in Tracks 5 and 6.

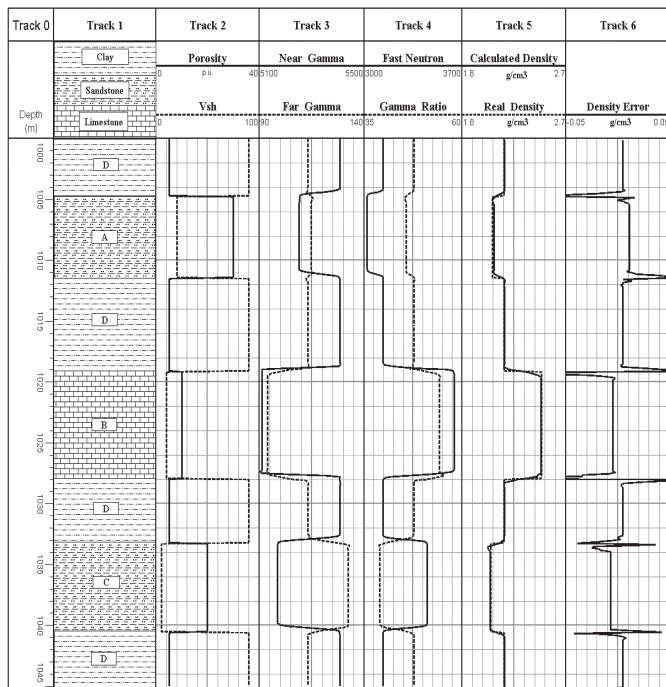


Fig. 15—Results of the Monte Carlo simulation.

From Fig. 15, we see that the near and far gamma-count curves (Track 3) and the inelastic-gamma-ratio curve (Track 4) are different for the formation layers with different porosity, density and minerals. The new density algorithm performs very well in a variety of mineralogies and gas-filled formations, and the density results from the new density algorithm (Track 5) are in good agreement with actual formation density without requiring correction.

CONCLUSIONS

In this paper, the coupled field concept is applied to the NGD measurement. Based on theory of fast-neutron scattering and gamma attenuation, fast-neutron gamma coupled field theory is proposed to describe the inelastic gamma field distribution, which can clarify the mathematic relationship of inelastic gamma field distribution, inelastic scattering cross section, fast-neutron scattering free path, density and other parameters. Applying the coupled theory, a new formation density algorithm was developed using the inelastic gamma-count ratio and the fast-neutron count is obtained, which avoids the need for HI correction and simplifies the data processing.

The new formation-density algorithm derived from fast-neutron gamma coupled field theory is verified with Monte Carlo simulation in a test well. The results are in good agreement with the benchmarked formations.

ACKNOWLEDGMENTS

The authors would like to acknowledge the assistance of the National Natural Science Foundation of China (41374125, 41574119, and 41504099), the National Major Oil and Gas Special Fund of China (2017ZX05019005-004), the Natural Science Foundation of Shandong Province (ZR2015DQ003) and the Special Fund of Central College Basic Research Operating Expenses (15CX06008A, 16CX02011A, 17CX02070).

NOMENCLATURE

Abbreviations

- D-T = deuterium-tritium
- ENDF = Evaluated Nuclear Data File
- GGD = gamma-gamma density
- HI = hydrogen index
- HSE = health, safety, and environmental
- LWD = logging-while-drilling
- MCNP = Monte Carlo N-particle code
- NGD = neutron gamma density
- p.u. = porosity units
- XCOM = photon cross sections database

Symbols

- CH_4 = chemical formula of methane gas
- $dI(r)$ = number of inelastic gamma photons generated in the spherical shell
- $d'I(r)$ = number of gamma photons from the spherical shell and recorded by detector A
- dr = thickness of the spherical shell
- $f(\lambda_s)$ = intercept of density curve
- i = average number of gamma photons from inelastic collisions of a fast neutron
- $I'(R)$ = total number of gamma photons detected by the detector A
- L = detector spacing
- L_1 = near-detector spacing
- L_2 = far-detector spacing
- L_3 = fast-neutron detector spacing
- r = distance from the source
- R = distance from the source to detector (detector spacing)
- R_0 = special detector spacing where the density attenuation and inelastic scattering cross section reach a balance
- R_∞ = radius of the spherical formation
- S_0 = neutron source strength
- V_{sh} = shale content
- ϕ = formation porosity
- λ_s = fast-neutron scattering free path

α	= proportional coefficient
α_1	= proportional coefficient of the near detector
α_2	= proportional coefficient of the far detector
ζ	= proportional coefficient
ρ	= formation density
ρ_{ma}	= formation matrix density
ρ_w	= formation water density
J_f	= fast-neutron flux
J_{in}	= inelastic-gamma flux
J_{in1}	= gamma count of the near detector
J_{in2}	= gamma count of the far detector
J_{inner}	= gamma count contributions of the formation inside
J_{outer}	= gamma count contributions of the formation outside the detector
Σ_{in}	= inelastic scattering cross section
$\Sigma_{in,w}$	= inelastic scattering cross sections of water
$\Sigma_{in,ma}$	= inelastic scattering cross sections of formation matrix
μ_m	= mass-attenuation coefficient

REFERENCES

- Alakeely, A., and Meridji, Y., 2014, Can Sourceless Density LWD Replace Wireline in Exploration Wells? Case Study from Saudi Arabia, Paper SPE-172178 presented at the SPE Saudi Arabia Section Technical Symposium and Exhibition, Al-Khobar, Saudi Arabia, 21–24 April. DOI: <https://doi.org/10.2118/172178-MS>
- Badruzzaman, A., 2014, An Assessment of Fundamentals of Nuclear-Based Alternatives to Conventional Chemical-Source Bulk Density Measurement, *Petrophysics*, **55**(5), 415–434.
- Badruzzaman, A., Badruzzaman, T., Zalan, T.A., and Mai, K., 2004, Multi-Sensor Through-Casing Density and Saturation Measurement Concepts With a Pulsed Neutron Source: A Modeling Assessment, Paper-89884 presented at the SPE International Petroleum Conference in Mexico, Puebla Pue, Mexico, 7–9 November. DOI: <https://doi.org/10.2118/89884-MS>
- Berger, M.J., Hubbell, J.H., Seltzer, S.M., Chang, J., Coursey, J.S., Sukumar, R., Zucker, D.S., and Olsen, K., 2010, *XCOM: Photon Cross Sections Database*, (Version1.5), Report NBSIR 87-3597, U.S. National Institute of Standards and Technology, Gaithersburg, Maryland. <http://physics.nist.gov/xcom>. Accessed July 7, 2017.
- Briesmeister, J.F., Editor, 1986, *MCNP-A General Monte Carlo Code for Neutron and Photon Transport, Version 3A*. Report No. LA-7396-M-Rev.3A, Los Alamos National Laboratory, Los Alamos, New Mexico. http://www.iaea.org/inis/collection/NCLCollectionStore/_Public/18/044/18044302.pdf. Accessed July 7, 2017.
- Chadwick, M.B., Obložinský, P., Herman, M., Greene, N.M., et al., 2006, ENDF/B-VII.0: Next Generation Evaluated Nuclear Data Library for Nuclear Science and Technology, *Nuclear Data Sheets*, **107**(12), 2931–3060. DOI: <https://doi.org/10.1016/j.nds.2006.11.001>
- Evans, M., Allioli, F., Cretoiu, V., Haranger, F., Laporte, N., Mauborgne, M.-L., Nicoletti, L., Reichel, N.J., Stoller, C., Tarrius, M., and Griffiths, R.J., 2012, Sourceless Neutron-Gamma Density (SNGD): A Radioisotope-Free Bulk Density Measurement: Physics Principles, Environmental Effects, and Applications, Paper SPE-159334 presented at the SPE Annual Technical Conference and Exhibition, San Antonio, Texas, USA, 8–10 October.
- Gardner, R.P., and Xu, L., 2009, Status of the Monte Carlo Library Least-Squares (MCLLS) Approach for Non-Linear Radiation Analyzer Problems, *Radiation Physics and Chemistry*, **78**(10), 843–851. <https://doi.org/10.1016/j.radphyschem.2009.04.023>
- Inanc, F., 2014, Pulsed Neutron Generator-Driven Sourceless Density Measurements—Expectations, Physics and Issues, Paper HHHH, *Transactions, SPWLA 55th Annual Logging Symposium*, Abu Dhabi, United Arab Emirates, 18–22 May.
- Jacobson, L., Durbin, D., Reed, S., 2004, An Improved Formation Density Measurement Using PNC tools, Paper SPE-90708 presented at the SPE Annual Technical Conference and Exhibition, Houston, Texas, 26–29 September.
- Liu, J., Zhang, F., Wang, X., Han, F., and Yuan, Z., 2014, Numerical Study on Determining Formation Porosity Using a Boron Capture Gamma Ray Technique and MCNP, *Applied Radiation and Isotopes*, **94**, 266–271. DOI: <https://doi.org/10.1016/j.apradiso.2014.08.013>
- Liu, J., Zhang, F., Gardner, R.P., Zhang, Q.Y., Hou, G., Zhang, H., and Ding, F., 2016, A Method of Improving Sensitivity of Carbon/Oxygen Well Logging for Low Porosity Formation, *Journal of China University of Petroleum*, **40**(6), 57–62. DOI: [10.3969/j.issn.1673-5005.2016.06.007](https://doi.org/10.3969/j.issn.1673-5005.2016.06.007)
- Mirto, E., Weller, G., El-Halawani, T., Grau, J.A., Berheide, M., Allioli, F., Evans, M., Berto, R., Borghi, M., Firini, Mauro, and Giorgioni, M., 2006, New Developments in Sourceless Logging While Drilling Formation Evaluation: A Case Study from Southern Italy, Paper SPE-100351 presented at the SPE Europec/EAGE Annual Conference and Exhibition, Vienna, Austria, 12–15 June. DOI: <https://doi.org/10.2118/100351-MS>
- Neuman, C.H., Sullivan, M.J., and Belanger, D.L., 1999, An Investigation of Density Derived From Pulsed Neutron Capture Measurements, Paper SPE-56647 presented at the SPE Annual Technical Conference and Exhibition, Houston, Texas, 3–6 October. DOI: <https://doi.org/10.2118/56647-MS>
- Oden, C.P., Schweitzer, J.S., McDowell, G.M., 2006, The feasibility of Well- Logging Measurements of Arsenic Levels Using Neutron-Activation Analysis, *Applied Radiation and Isotopes*, **64**(9), 1074–1081. DOI: <https://doi.org/10.1016/j.apradiso.2006.04.007>
- Odom, R.C., Bailey S.M., Wilson, R.D., and Archer, M.P., 1999, Pulsed Neutron Density Measurements: Modeling the Depth of Investigation and Cased-Hole Wellbore Uncertainties, Paper JJ, *Transactions, SPWLA 40th Annual Logging Symposium*, Oslo, Norway, 30 May–3 June.
- Odom, R. C., Tiller, D.E., and Wilson, R.D., 2001a, Improvements in a Through-Casing Pulsed-Neutron Density Log, Paper SPE-71742 presented at the SPE Annual Technical Conference

- and Exhibition, New Orleans, Louisiana, 30 September–3 October. DOI: <https://doi.org/10.2118/71742-MS>
- Odom, R.C., Wilson, R.D., and Ladtkow, R.K., 2001b, Log Examples With a Prototype Three-Detector Pulsed- Neutron System for Measurement of Cased-Hole Neutron and Density Porosities, Paper SPE-71042 presented at the SPE Rocky Mountain Petroleum Technology Conference, Keystone, Colorado, 21–23 May. DOI: <https://doi.org/10.2118/71042-MS>
- Panzner, M., Morten, J.P., Weibull, W.W., and Arntsen, B., 2016, Integrated Seismic and Electromagnetic Model Building Applied to Improve Subbasalt Depth Imaging in the Faroe-Shetland Basin, *Geophysics*, **81**(1), E57–E68. DOI: <https://doi.org/10.1190/geo2015-0137.1>
- Reichel, N., Evans, M., Allioli, F., Mauborgne, M.-L., Nicoletti, L., Haranger, F., Laporte, N., Stoller, C., Cretoiu, V., El-Hehiawy, E., and Rabe, R., 2013, Sourceless Neutron-Gamma Density (SNGD): Principles, Field-Test Results and Log Quality Control of a Radioisotope-Free Bulk-Density Measurement, *Petrophysics*, **54**(2), 91–103.
- Smith H.D., Jr., Duenckel, R., and Han, X., 2013, A New Nuclear Logging Method to Locate Proppant Placement in Induced Fractures, *Petrophysics*, **54**(5), 415–426.
- Tittle, C.W., 1961, Theory of Neutron Logging I, *Geophysics*, **26**(1), 27–39. DOI: <https://doi.org/10.1190/1.1438839>
- Weller, G., Griffiths, R., Stoller, C., Allioli, F., Berheide, M., Evans, M., Labous, L., Dion D., and Perciot, P., 2005, A New Integrated LWD Platform Brings Next-Generation Formation Evaluation Services, Paper H, *Transactions, SPWLA 46th Annual Logging Symposium*, New Orleans, Louisiana, USA, 26–29 June.
- Xu, L., Schultz, W., Huiszoon, C., 2010, A Comprehensive Investigation of Source Effects on Neutron Porosity Response for Logging-While-Drilling Measurements, *Petrophysics*, **51**(3), 185–198.
- X-5 Monte Carlo Team, 2008, *MCNP – A General Monte Carlo N-Particle Transport Code, Version 5, Volume 1: Overview and Theory*, Report LA-UR-03-1987, Los Alamo National Laboratory, Los Alamos, New Mexico, USA. https://laws.lanl.gov/vhosts/mcnp.lanl.gov/pdf_files/la-ur-03-1987.pdf. Accessed July 7, 2017.
- Yu, P., Geng, J., Li, X., and Wang, C., 2016, Acoustic-Elastic Coupled Equation for Ocean Bottom Seismic Data Elastic Reverse Time Migration, *Geophysics*, **81**(5): S333–S345. DOI: <https://doi.org/10.1190/geo2015-0535.1>
- Zhang, F., Yuan, C., Liu, J., and Jia, Y., 2013, Numerical Simulation on Pulsed Neutron-Gamma Ray Density Logging Response in Logging While Drilling, *Earth Science*, **38**(5), 1116–1120. DOI: [10.3799/dqkx.2013.110](https://doi.org/10.3799/dqkx.2013.110)

ABOUT THE AUTHORS

Quanying Zhang is a PhD student in Geological Resources and Geological Engineering of China University of Petroleum (East China). His research involves the Monte Carlo simulation, nuclear well logging, data processing

and interpretation, particularly in the theory and method of pulsed-neutron-gamma density logging. In addition, he is also a member of the Nuclear Well Logging Group in China University of Petroleum (East China)

Feng Zhang is Director of Nuclear Well Logging Group in China University of Petroleum (East China). He is a professor in School of Geosciences, China University of Petroleum (East China). His research primarily involves tool design, study methods, data processing of nuclear well logging. He holds a PhD in Geological resources and Geological Engineering from China University of Petroleum (East China). He has published more than 90 academic papers, applied for 20 China patents and three software copyrights. Professor Zhang has been engaged in research of nuclear logging for 20 years, and his achievements include the first-place award in science and technology progress from Henan Province of China, the third-place award in science and technology progress from Shandong Province of China.

Juntao Liu is an assistant professor in China University of Petroleum (East China) and his research interests include modeling of nuclear well logs (including Monte Carlo simulation and fast approximate numerical simulation), data processing and software development. He holds a PhD in Geological Resources and Geological Engineering from China University of Petroleum, and has published 15 academic papers and been granted five China patents. He is a member of SPWLA, SPE, EAGE and SEG.

He Wu obtained his BS degree in nuclear engineering and technology from Chengdu University of Technology, China. He is currently a PhD Student at China University of Petroleum and his research interests include both density and elemental well logging methods. He is a member of the Nuclear Well Logging Group in China University of Petroleum (East China) member of SPWLA and SPE.

Guoli Wu is a teacher in School of Geosciences, China University of Petroleum (East China). She holds a PhD from the University of Chinese Academy of Sciences. Her primary area of research is in physical oceanography and numerical solutions of inverse problems.

Wenbao Jia is a professor in College of Materials Science and Engineering, Nanjing University of Aeronautics and Astronautics. His research interests include the interaction of radiation and materials, and industry application of radiation effect. He has published more than 30 academic papers and

holds several patents. Professor's Jia achievements include third-place award for science and technology progress from Gansu Province of China.

Yongzhou Ti is a Senior Engineer in Zhengzhou Key Laboratory of Isotope Tracing and Detecting, Isotope Research Institute of Henan Academy of Sciences Co. Ltd. His primary area of research is the theory of isotope logging.

Jing Li is a teacher in Department of Biology, Gutu Branch School of Mongolian Senior High School. She holds a Bachelors degree in Shenyang Normal University. Her primary area of research is biology. She is a member of EAGE and SEG.